High-performance and long-term stability of mesoporous Cu-doped TiO_2 microsphere for catalytic CO oxidation

Wen-Ta Yang [a,b], Chin Jung Lin [c], Tiziano Montini [d], Paolo Fornasiero [d], Sofia Ya [a,b,c,d], Sofia Ya Hsuan Liou [a,b,*]

[a] Department of Geosciences, National Taiwan University, Taipei 106, Taiwan
[b] Research Center for Future Earth, National Taiwan University, Taipei 106, Taiwan
[c] Department of Environmental Engineering, National I-Lan University, I-Lan 260, Taiwan
[d] Department of Chemical and Pharmaceutical Sciences, University of Trieste, 34127 Trieste, Italy

ARTICLE INFO

Editor: L. Eder

Keywords:
Cu-O-Ti
well-dispersed
real-time mass
one-step AASA

ABSTRACT

Although the low-temperature reaction mechanism of catalytic CO oxidation reaction remains unclear, the active sites of copper play a crucial role in this mechanism. One-step aerosol-assisted self-assembly (AASA) process has been developed for the synthesis of mesoporous Cu-doped TiO_2 microspheres (CuTMS) to incorporate copper into the TiO_2 lattice. This strategy highly enhanced the dispersion of copper from 41.10 to 83.65%. Long-term stability of the as-synthesized CuTMS materials for catalytic CO oxidation reaction was monitored using real-time mass spectrum. Isolated CuO and Cu-O-Ti were formed as determined by X-ray photoelectron spectroscopy (XPS). The formation of the Cu-O-Ti bonds in the crystal lattice changes the electron densities of Ti(IV) and O, causing a subsequent change in Ti(III)/Ti(IV) and O_{non}/O_{Total} ratio. 20CuTMS contained the highest lattice distortion (0.44) in which the O_{non}/O_{Total} ratio is lowest (0.18). This finding may be attributed to the absolute formation of the Cu-O-Ti bonds in the crystal lattice. However, the decrease of Ti(III)/Ti(IV) ratio to about 0.35 of 25CuTMS was caused by the CuO cluster formation on the surface. N_2O titration-assisted H_2 temperature-programmed reduction and in-situ Fourier transform infrared spectroscopy revealed the properties of copper and effects of active sites.

1. Introduction

Poor ambient air quality is a serious threat to human health in urban areas. Toxic compounds, such as volatile organic compounds and CO, are emitted from motor vehicles and industrial smokestacks because of incomplete fuel combustion. Catalytic oxidation, which is used to clean emissions, is a promising technology necessary for converting pollutants into CO_2 and H_2O (Srivastava et al., 2012). Harmful gases from cars pollute the environment before a catalytic converter reaches the operating temperature of catalysts to achieve complete conversion. Environmental regulations have been strengthened to convert effectively exhaust pollutants from industrial and transport sources. Thus, highly efficient catalysts for removing CO and other pollutants are in great demand. The catalysts supported by noble metals, such as Au (Li et al., 2020), Pd (Murata et al., 2019), Pt (Ma et al., 2019), and Rh (Zhang et al., 2019), exhibit high activity for catalytic CO oxidation. Noble metal-based catalysts are reactive at ultra-low temperatures (from 0 ℃ to liquid nitrogen temperature) owing to the nature of noble metals and dispersion (DeRita et al., 2017; Nie et al., 2017).

However, nanocatalysts easily agglomerate to form large entities, the catalytic activity of which drastically decrease, especially at high temperatures (Shokouhimehr et al., 2018; Lee et al., 2005; Kaminski et al., 2015). Consequently, the application of noble materials is limited by their low natural abundance, low working temperatures (Seo et al., 2010; Liu et al., 2012; Guan et al., 2016), chemical states (Seo et al., 2010; Newton et al., 2015; Guan et al., 2016), and metal dispersion (Suchomel et al., 2018; Zhang et al., 2019; Li et al., 2020). Catalysts based on the nanostructures of non-noble metals, such as Cu, Mn (Mo et al., 2019), and Ni (Gao et al., 2016) compounds, are cost-effective catalytic CO oxidation catalysts. In particular, copper-containing materials exhibit great performance in low-temperature conversion of CO to CO_2 (Svintsitskiy et al., 2013; DeSario et al., 2019) at a high space velocity (over 36,000 h^{-1}) (Zhang et al., 2016).

In general, catalytic CO oxidation is significantly correlated with the

* Corresponding author at: Department of Geosciences, National Taiwan University, Taipei 106, Taiwan.
E-mail address: yhliou@ntu.edu.tw (S.Y.H. Liou).

Accepted 3 August 2020

state of the doped metal, defect structure, active sites, and interaction between the doped metal and the supporter. Kim and Liu (2015) reported that in TiO_2-supported copper materials, the surface structure between copper and titanium provides multiple components for catalytic CO oxidation. The active sites of catalytic CO oxidation occur on the surface of copper oxides and support TiO_2 and in the step edge between copper and TiO_2. Highly dispersing the doping metal onto the supporter is necessary to increase the exposure of surface copper or the step edge of copper and TiO_2 matrix.

The development of highly dispersed catalysts is challenging. Conventional preparation methods for producing highly dispersed metals and metal oxides are inefficient and time consuming (Lin et al., 2015; Ryu et al., 2015). Aerosol-assisted self-assembly (AASA) is a large-scale and productive method for synthesizing highly porous materials (Ryu et al., 2015; Fu et al., 2017). This process was first developed to obtain mesoporous silica-based materials (Lu et al., 1999). Tsung et al. (2008) used the acetate mediation system to produce metal alkoxides to synthesize non-silica metal oxides. Doping metal oxides with metals as bimetallic materials has been reported. Catalytically active nanostructures are incorporated into mesoporous supports to increase the dispersion of nanocatalysts. The one-step method is used to modify the synthesis procedure. This method provides an effectively controllable process for synthesizing metals and metal oxides with a strong interaction (Hampsey et al., 2005; Lin et al., 2015; Lin and Yang, 2014). Compared with the post-incorporation process, the one-step AASA prevents pore blocking and doping copper aggregation. The high dispersion of copper, which enhances the interfacial interaction of copper and titanium oxide, was found to be due to the formation of oxygen vacancy and under-coordinated sites (Kwak et al., 2009; Seriani et al., 2015; Lee et al., 2016).

The present work investigated the coexisting copper species of CuTMS synthesized via a one-step AASA process. Previously, less amount of copper was used to modified the electron structure of TiO_2 as visible-light-driven photocatalyst (Lin and Yang, 2014). And now copper plays a role of thermal catalyst and TiO_2 as support for catalytic CO oxidation. An in situ technique was adopted to evaluate the effects of active sites on the copper/titanium system material. The dispersion and physicochemical properties of Cu species in TiO_2 was investigated using N_2O titration-assisted H_2-TPR. The interaction between CO and Cu in TiO_2 was observed using in-situ FTIR. The temperature-dependence of turnover frequency (TOF) was evaluated to determine the contribution of the active sites. The as-synthesized material exhibited remarkable performance and long-term stability compared with commercial CuO. The goal of this work is providing a potentially catalytic CO oxidation candidate for manufacturing three-way catalytic converters.

2. Materials and methods

2.1. One-step AASA (Material) synthesis

All chemicals used were of analytical or reagent grade without further purification and purchased from Sigma-Aldrich, Fluka, and Nacalai Tesque Inc. Milli-Q water (Sartorius) was employed throughout the experiments. The precursor was homogeneously mixed with tetrabutyl titanate ($Ti[OBu]_4$, 98%):acetic acid (>99%):hydrochloride acid (HCl, 37%):ethanol (absolute, >99.8%):Polyethylene-polypropylene glycol (F127) at a 1:4:1.2:20:0.01 ratio. For copper-doped material, the adapting copper loading was used (the one-step strategies. In the Cu/TiO_2 material, the ratio of $(Cu[NO_3]_2{\cdot}2.5H_2O)$/ethanol stock solution was adjusted for load systematically appropriate amounts of copper ranging from ion ratios of 3.0, 10, 20, and 25 relative to the presence of titanium ions. The sols were aged at ambient temperature for 2 h and stirred at 400 rpm by using an air compressor as a driving force that feeding aerosol into a spherical atomizer (D = 200 mm). The liquid constituents were rapidly volatilized, and the droplets were transferred through a quartz tube furnace at 400 °C with a back-end ultra-vacuum pump. The dry powder was collected on a cellulose acetate membrane filter (0.45 μm) and calcined at 400 °C (ramp 2 °C/min) in air flow for 5 h to remove the templet F127 and to induce crystalline TiO_2. Hereafter, the obtained TiO_2 mesosphere is denoted as TMS. The copper-modified materials are labeled as XCuTMS, where X is the percentage of copper/titanium ratio in mole.

2.2. Material characterization

The prepared TMS and CuTMS samples were characterized. The morphology and elemental distribution of the samples were examined under a field-emission scanning electron microscope (FE-SEM) (JEOL JSM-6500 F) fitted with an energy dispersive X-ray spectrometer. Crystalline structures were analyzed using a D8 DISCOVER SSS multifunction high-powered diffractometer and Cu-Kα radiation (λ =1.5405 Å).

Textural properties were measured by N_2 adsorption-desorption isotherms at liquid N_2 temperature by using a Micromeritics ASAP 2020 analyzer. X-ray photoelectron spectroscopy (XPS) was conducted using a VG Scientific ESCALAB 250 equipped with a monochromated XR5 X-ray and aluminum target (15 kV) measurement of electron spectroscopy for chemical analysis system. Photoelectrons were collected from a take-off angle of 90° relative to the sample surface. The photoelectrons were then analyzed to ensure the element-binding energies of Ti 2p, O 1s, and Cu 2p.

2.3. Hydrogen temperature-programmed reduction (H_2-TPR)

To estimate the surface area, particle size, and dispersion of metallic copper properties, a hydrogen TPR reaction combined with nitrous oxide oxidation was performed in a U-shaped quartz reactor at atmospheric pressure (Gervasini and Bennici, 2005; Lai et al., 2018). Fresh CuTMS (200 mg) was loaded on 40 mesh silica bed with a steam rate of 60 ml/min (5% H_2 balance with Ar) and heated at 10 °C/min to reach the first H_2-TPR result. First, hydrogen consumption was X, in which copper oxide species was reduced to Cu(0) ($CuO + H_2 \rightarrow Cu + H_2O$). Subsequently, the mixed steam was switched to 5% N_2O in Ar for 1 h when the system temperature remained constant at 90 °C. According to the reaction $2Cu + N_2O \rightarrow Cu_2O + N_2$, nitrous oxide reoxidized Cu(0) to Cu(I). Second, hydrogen consumption after N_2O exposure was Y: ($Cu_2O + H_2 \rightarrow 2Cu + H_2O$). In the cooling procedure, argon was flowed to prevent reoxidation on every batch of experiments. The copper dispersion (D_{Cu}) was calculated using Eq. (1) to determine the ratio of surface copper and total copper in the material system. For the surface area (S_{Cu}), the contribution from metallic copper was determined using Eq. (2). Approximately 1.47×10^{19} (atoms·m^{-2}) was assumed as the constant of average surface density for the metal. Theoretically, the TPR results were used to evaluate the copper particle size (d_{Cu}) by assuming that copper particles have a spherical shape in Eq. (3).

$$D_{Cu}(\%) = \frac{2Y}{X} \times 100\% \tag{1}$$

$$S_{Cu}(m^2 g^{-1}) = \frac{2Y \times N_{av}}{X \times M_{Cu} \times 1.47 \times 10^{19}} \tag{2}$$

$$d_{Cu}(\mathrm{nm}) = \frac{6}{S_{Cu} \times \rho_{Cu}} \tag{3}$$

N_{av} : *Avogadro's constant* $= 6.02 \times 10^{23}\ mol^{-1}$

M_{Cu} : *Relative atomic mass of copper* $= 63.546\ g{\cdot}mol^{-1}$

ρ_{Cu} : *Density of motallic copper* $= 8.92\ g{\cdot}cm^{-3}$

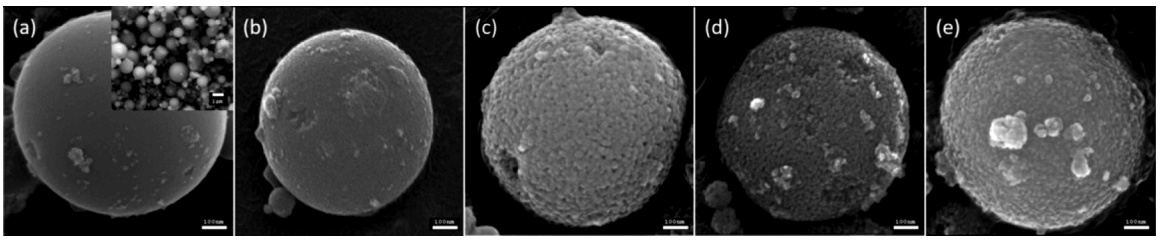

Fig. 1. SEM images of the surface morphology of (a) TMS, (b) 3.0CuTMS, (c) 10CuTMS, (d) 20CuTMS, and (e) 25CuTMS follow copper loading.

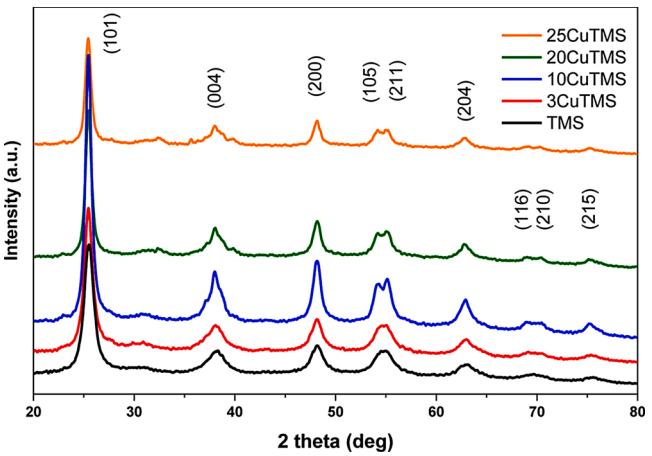

Fig. 2. Full-range XRD patterns of the as-prepared TMS and copper containing CuTMS mesoporous microsphere.

2.4. Insitu diffuse reflectance infrared Fourier transform spectroscopy (DRIFTS)

In situ DRIFTS was performed using an Interspectrum spectrometer (200-X) equipped with a deuterated triglycine sulfate detector operating at 1 cm^{-1} resolution. A total of 32 scans were collected within the range of 400-4000 cm^{-1}. The samples were transferred to a DiffusIR heating cartridge (PIKE) assisted with KBr windows (DI is 32 mm and thickness is 3 mm) and non-oil vacuum pump (Edwards). Following the same procedure before every catalytic CO oxidation test, CuTMS was pre-treated with 5% oxygen in argon, heated to 300 °C, and then purged with argon for 1 h to remove residual gases before performing the measurements. CuTMS was loaded into the cell and heated to 250 °C to trace the changes in binding groups on the material surface. During this procedure, the DRIFTS recorded the controlled atmosphere as described in the catalytic CO oxidation process.

2.5. Catalytic CO oxidation activity and stability test

For catalytic CO oxidation, gas steam mix, pulse, and exposure were controlled by a Brooks mass flow controller (0254) equipped with a flow meter (5850E). All batches of 36 mg of CuTMS reaction were placed in a double-layer quartz bed in a U-shaped silica tube reactor and then pretreated with 5% O_2 in 40 ml/min argon (10 °C/min) at 300 °C for 30 min before catalytic CO oxidation. During the cooling procedure, pure argon was introduced into the reactor to remove residual gas and prevent atmospheric intrusion. Material activity test was operated from room temperature to 250 °C (2 °C/min) for 1 h under 1:1 CO:O_2 ratio in argon (GHSV = 100,000 h^{-1}). Real-time results were determined by quadrupole mass spectrometry (Hiden HPR-20 R&D) equipped with a quartz inert capillary inlet working at 180 °C. Stability tests of the materials were run in accordance with the abovementioned pretreatment and catalytic CO oxidation processes. The temperature was increased to 10 °C/min and maintained at 250 °C for 200 h to measure the thermal stability of commercial copper oxide and the as-prepared CuTMS.

Table 1
Summary of the textural properties of CuTMS samples calcined in compressed air flow for 5 h at 400 °C.

Sample	S_{BET} (m^2 g^{-1})[a]	Pore Size (nm)[b]	Pore volume (cm^3 g^{-1})	Crystallite size (nm)[c]
TMS	199	5.6	0.2982	7.1
3.0CuTMS	186	5.7	0.2493	8.5
10CuTMS	102	7.9	0.2227	11.2
20CuTMS	86	6.3 / 12.5	0.2039	11.2
25CuTMS	81	6.2 / 14.1	0.1926	11.5

[a] Calculated from the linear part of the BET plot.
[b] Estimated by the BJH formula using the adsorption branch of the isotherm.
[c] Scherrer equation.

3. Results and discussion

3.1. Morphology and characterization of CuTMS

The as prepared TMS and CuTMS materials via one-step AASA showed a considerable change in color from slightly yellow to yellow-green as the copper/titanium molar ratio increased (Fig. S1). The SEM images of collected sample via one-step AASA sprayed is provided in Fig. S2. The SEM images are shown in Fig. 1. Fig. 1(a) and the inserted graph exhibit typical microsphere morphologies of the as-synthesized TMS with particle size of 1-2 μm, the particle size histogram as shown in Fig. S3. The elemental signals of copper and titanium were detected by EDX analysis were providing in Fig. S4. Notably, the TMS surfaces were free of cracks before copper loading. In Figs. 1(c) to 1(e), the materials showed an obvious roughness with visible granular features on the surface. As shown in the XRD pattern in Fig. 2, the common peaks of TMS and CuTMS were observed at 2θ of 25.3°, 37.8°,48.0°, 53.8°, 54.9°, and 62.7°, which represented the diffraction peaks of the (101), (004), (200), (105), (211), and (204) crystal planes, as a typical anatase phase of TiO_2 (JCPDS 21-1272). The average sizes of anatase TiO_2 crystallite were estimated by using the Scherrer equation (Table 1). The results showed that the crystal size of anatase growth followed copper loading. Several studies reported that metal ions promote the formation of crystallization (Zhang et al., 2004; Mehrmohammadi et al., 2011; Zeng et al., 2017). It is noted that the diffraction peaks decrease on 20CuTMS and 25CuTMS samples which is due to the lower structural quality. Furthermore, the absence of characteristic peaks of cuprous oxide and cupric oxide species are due to small particle size and well-dispersed copper (Park et al., 2017; Putrakumar et al., 2015). Both phenomena indicated that the formation of defects, which suggested that a strong interaction might exist between copper and TiO_2. (Choudhury et al., 2013) With increasing Cu content, the peaks slightly broaden and the crystallite sizes are increasing, indicating a slight distortion in the crystal structure. The formation of crystallographic point defects due to the substitution of Ti^{4+} by Cu^{2+} may cause the diffraction peaks intensity decreased with increasing the copper incorporation to 20CuTMS and 25CuTMS. Most copper ions might be inserted into the structure of TiO_2 located at the interstice. The nitrogen adsorption measurements

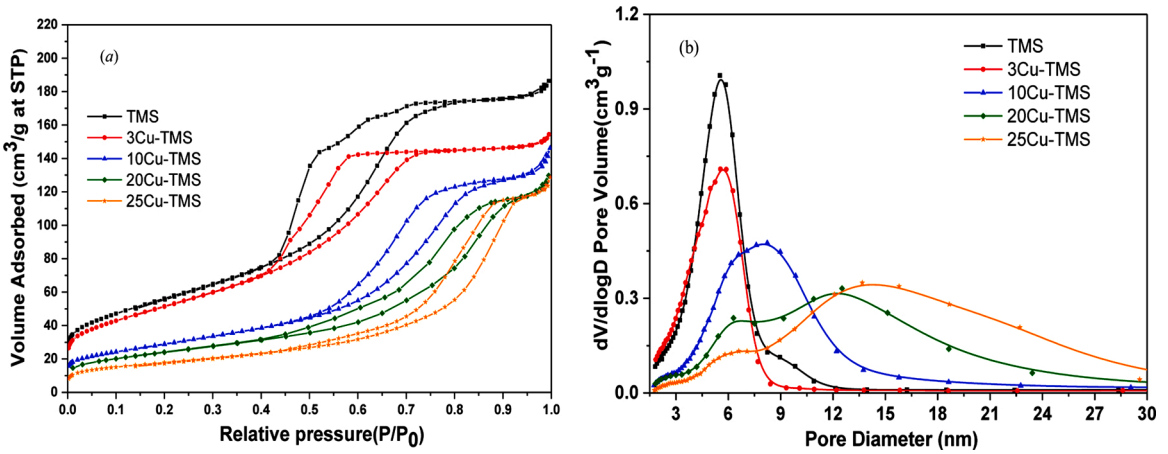

Fig. 3. Nitrogen adsorption–desorption isotherms of CuTMS after calcination at 400 °C (a) and the corresponding pore size distribution curve calculated using the BJH equation in the adsorption branch of the nitrogen isotherm (b).

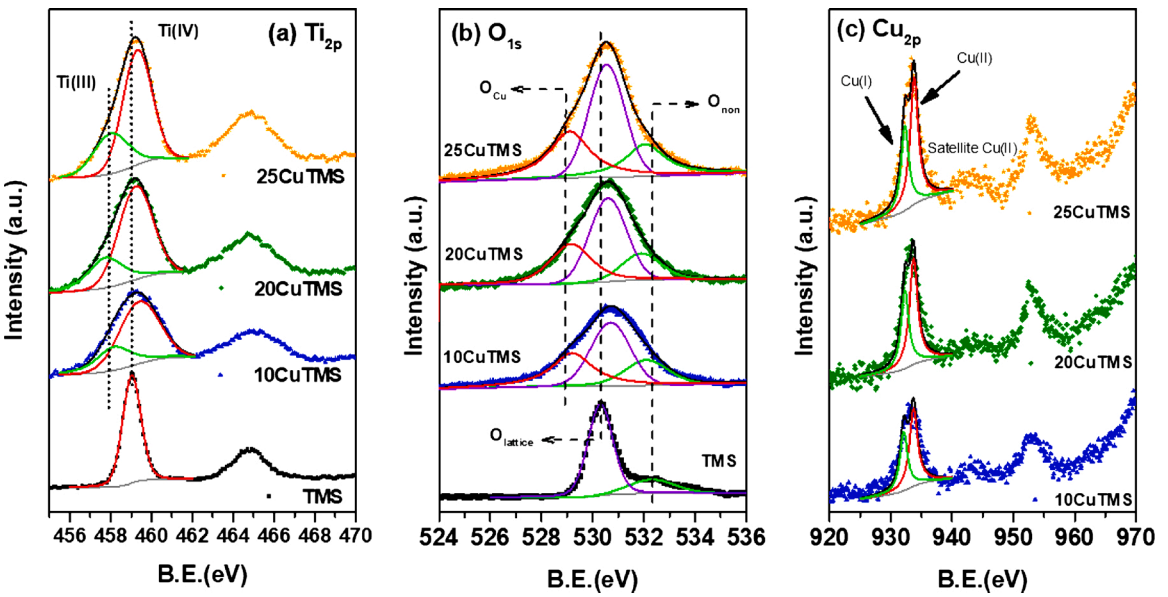

Fig. 4. Deconvolution of high-resolution XPS spectra on catalysts with various copper contents: (a) Ti2p, (b) O 1s, and (c) Cu 2p.

demonstrate that all the materials exhibit the type IV isotherm behavior (Fig. 3a), with high BET surface areas ranging from 81 m^2/g to 199 m^2/g of 25CuTMS to TMS (Table 1). The hysteresis loops of TMS and 3CuTMS were similar to H2(a)-type pore structures with steep desorption behavior at relative pressure P/P_0 of 0.4-0.6. A moderate desorption branch in 10CuTMS, 20CuTMS, and 25CuTMS materials, which represented H2(b) tunnel properties, was observed. Both H2-type materials were equipped with a pore-blocking structure; however, H2(b) had a larger size distribution of neck widths than H2(a). This isothermal desorption behavior matched with the material pore size distribution in Fig. 3(b). The pore size distribution was calculated by BJH, and the uptake of the adsorption branch is shown in Table 1. As expected, the pore size increased in materials containing high amounts of copper, especially 20CuTMS and 25CuTMS reveals the presence of two set of pores with size centered at 6.3 and 12.5 nm, 6.2 and 14.1 nm, respectively, which are significantly larger than that of the 10CuTMS. By contrast, the textural properties of CuTMS with anatase crystalline showed decreased pore volume, which was attributed to the growth of anatase crystalline that partially blocked the tunnel path. Similarly, the specific surface area decreased as the copper/titanium molar ratio increased. One-step strategy and appropriate calcination conditions facilitated the AASA method to prepare an ordered tunnel structure for CuTMS.

Determining the composition and chemical state on the surface of copper-doped TMS is crucial for understanding the catalytic CO oxidation reaction. The XPS spectra of the CuTMS are shown in Fig. 4. The peak positions of Ti $2p_{3/2}$ for TMS, 10CuTMS, 20CuTMS, and 25CuTMS were located at 459, 459.3, 459.2, and 459.3 eV, respectively (Fig. 4a). Notably, the binding energies of copper dopant samples shifted to higher energies in Ti $2p_{3/2}$ compared with TMS. A tailing peak at low energy (457.9 eV) was observed and ascribed to Ti(III) (Luo et al., 2018; Bharti et al., 2016). Xu et al. found that the formation of Ti^{3+} defects is attributed to lattice distortion, which enhances catalytic performance (Xu et al., 2017). The formation of the Cu-O-Ti bonds in the crystal lattice changes the electron densities of Ti(IV) and O, causing a subsequent change in Ti(III)/Ti(IV) and O_{non}/O_{Total} ratio. 20CuTMS contained the highest lattice distortion (0.44) in which the O_{non}/O_{Total} ratio is lowest (0.18). This finding may be attributed to the absolute formation of the Cu-O-Ti bonds in the crystal lattice. However, the decrease of Ti (III)/Ti(IV) ratio to about 0.35 of 25CuTMS was caused by the CuO cluster formation on the surface. The material element state and surface compositions are summarized in Table 2. The results of XPS O 1s

Table 2
Surface chemical state and composition of the calcined materials that were estimated from the result deconvolution of XPS.

Samples	Binding energy (eV)				Evaluated of atomic ratio		Evaluated theconcentration ofOxygen vacancy
	Cu_{2p} Cu(α)	Cu_{2p} Cu(β)	Ti_{2p} Ti(III)	Ti_{2p} Ti(IV)	Cu(β)/Cu(α + β)	Ti(III)/Ti(IV)	Onon[a]/OTotal[b]
TMS	—	—	—	459	—	—	0.20
10CuTMS	932.1	933.7	457.8	459.3	0.41	0.42	0.22
20CuTMS	932.3	933.7	457.8	459.2	0.41	0.44	0.18
25CuTMS	932.3	933.8	457.8	459.3	0.39	0.35	0.21

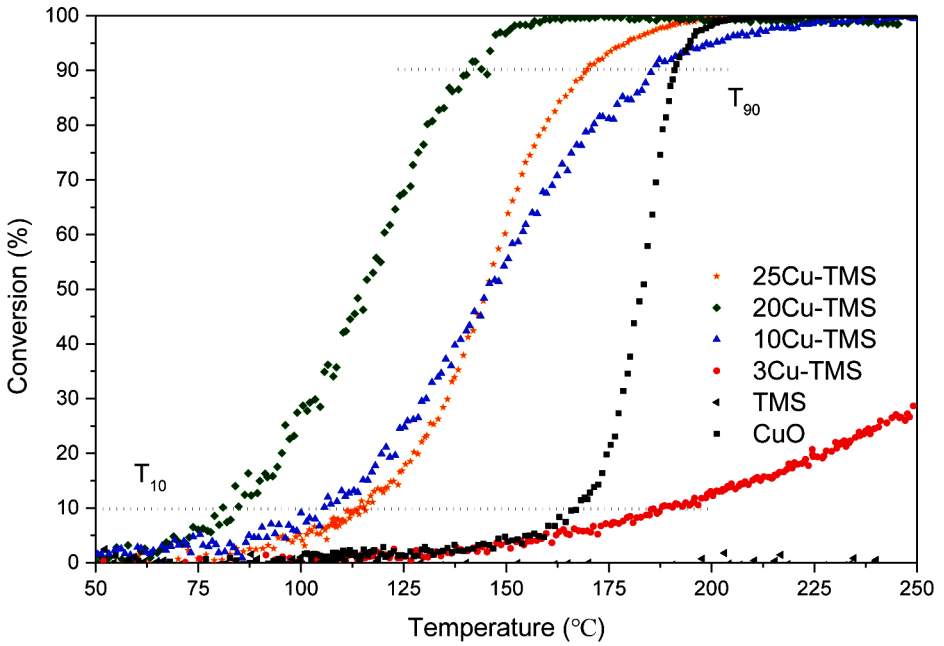

Fig. 5. Conversion rate of CuTMS catalytically oxidized CO with ramp rate of 2 °C/min against commercial CuO. Feed gas composition: 1% CO, 1%O_2 balance with argon (100,000 GHSV).

analysis (shown in Fig. 4(b)) are as follows: the characteristic peak consisted of a sharp peak and a wide weak peak, which are attributed to TiO_2 surface lattice oxygen (530 eV) and surface non-lattice oxygen centered at around 532 eV, respectively (Bharti et al., 2016). Peak tailing was due to the Cu-O bond at 529.2 eV. The deconvolution of O 1S was estimated for the peak area ratio of O_{non}/O_{total} to obtain information regarding oxygen vacancy (Naldoni et al., 2012; Tang et al., 2016). In Fig. 4(c) Cu $2p_{3/2}$ of copper-doped TMS, shake-up satellite peaks were observed between 940 eV and 945 eV. An asymmetric peak was overlapped by two peaks, centered at 932.1 and 933.7 eV, which were assigned to Cu(α) and Cu(β) (Wang et al., 2016). Cu(β) is highly related to the copper inserted into the structure of TiO_2 or might occupy some of the titanium lattice site. Cu(α) act as superficial copper on the surface. The (Cu(β)/Cu(α + β)) for 10CuTMS, 20CuTMS, and 25CuTMS were 0.41, 0.41, and 0.39, respectively. Therefore 25CuTMS shows more superficial copper than 10CuTMS, 20CuTMS. The formation of the Cu-O-Ti bonds in the crystal lattice changes the electron densities of Ti (IV) and O, causing a subsequent change in Ti(III)/Ti(IV) and O_{non}/O_{total} ratio. 20CuTMS contained the highest lattice distortion (0.44) in which the O_{non}/O_{total} ratio is lowest (0.18). This finding may be attributed to the absolute formation of the Cu-O-Ti bonds in the crystal lattice. However, the decrease of Ti(III)/Ti(IV) ratio to about 0.35 of 25CuTMS was caused by the CuO cluster formation on the surface. These results suggested the introduction of copper-substituted titanium in the TiO_2 lattice in which the structure of Cu-O-Ti formed (Choudhury et al., 2013; Dong et al., 2016; Pham and Lee, 2016).

3.2. CO oxidation performance and stability of CuTMS

The catalytic CO oxidation conversion rate of the as-synthesized CuTMS catalyst is shown in Fig. 5. In the TMS without CO conversion, the mass spectrum was detected at m/z = 44 (Fig. S5). No considerable counts above the background were detected, indicating the TMS bare without matrix effect. The ability of catalytic CO oxidation improved at various copper contents. The CO conversion of 3CuTMS was below 30% at 250 °C. The remaining three samples showed complete mineralization of CO to CO_2 (Fig. S5) at 160 °C, 195 °C, and 225 °C. 20CuTMS showed optimal copper loading conditions with the lowest T^a_{10} (84 °C) and T^b_{90} (140 °C). For comparison, a commercial CuO material (99.995%) (Alfa Aesar) was tested under the same condition and the same catalytic CO oxidation procedure described in Section 2.4. The commercial CuO powder exhibited a relatively low catalytic CO oxidation ability, and its T_{10} and T_{90} was located at 137 °C and 163 °C, respectively. Furthermore, 10CuTMS and 25CuTMS exhibited a similar performance; however, the conversion was reversed at T_{10} and T_{90}. CuTMS catalytic CO oxidation behavior has attracted great interest because reverse conversion occurs in 10CuTMS and 25CuTMS at a relatively low reaction temperature owing to the effects of active species that are strongly affected by temperature. The differences in CuTMS catalytic CO oxidation activity were investigated further. Reaction reversal occurred in 10CuTMS and 25CuTMS at a relatively high temperature. Therefore, the metal properties and active sites on the surface of 10CuTMS, 20CuTMS, and 25CuTMS were analyzed.

The stability test of catalytic CO oxidation of 20CuTMS and 25CuTMS was conducted at 250 °C (GHSV = 100,000 h^{-1}) to evaluate

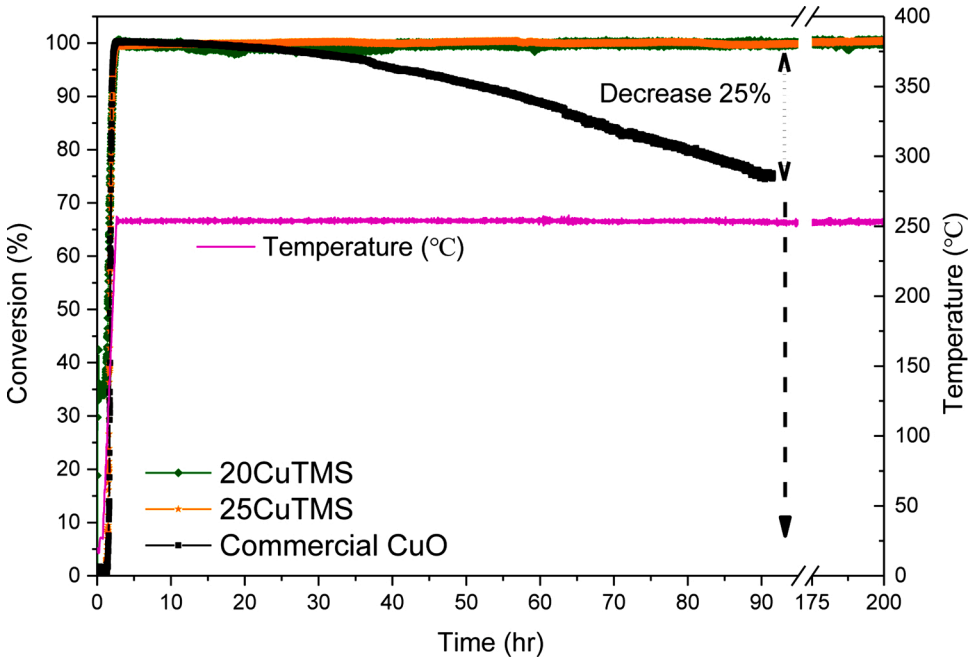

Fig. 6. Durability test of 20CuTMS and 25CuTMS catalysts compared with commercial CuO at a constant temperature of 250 °C for 200 h.

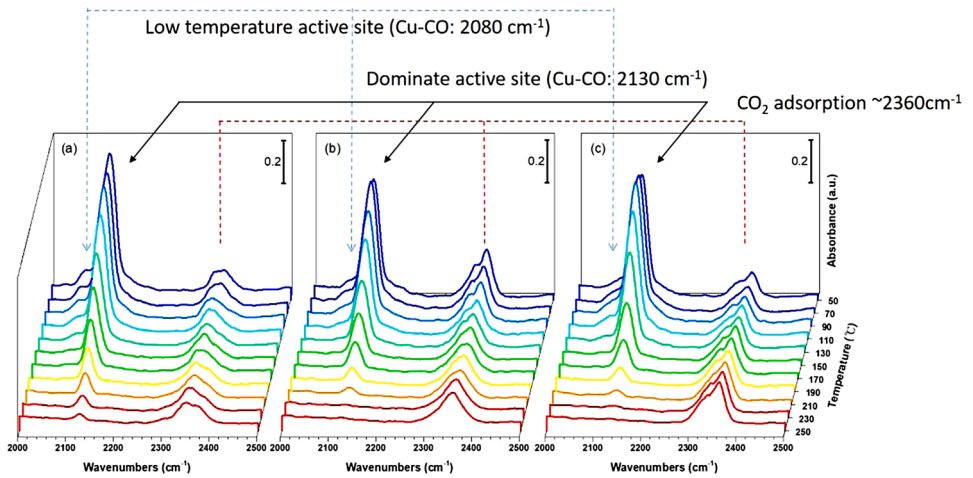

Fig. 7. In situ DRIFTS measurements under controlled CO/O_2 steam. The IR adsorption spectrum were uptake from 50 °C to 250 °C. (a) 10CuTMS, (b) 20CuTMS, and (c) 25CuTMS.

their long-term performance compared with that of commercial CuO. However, to the best of our knowledge, no stability test for catalytic CO oxidation under extreme conditions (e.g., 200 h real-time measurement) for evaluating CO tolerance has been developed. The stability of the commercial CuO considerably decreased compared with that of the as-prepared catalysts, wherein over 25% of CO conversion was observed at 90 h of reaction (Fig. 6). After 200 h of measurement, the stability of the as-prepared 20CuTMS and 25CuTMS did not substantially decrease. The thermal stability of the structures of the materials is shown in Fig. S6, which illustrates the XRD patterns of 10CuTMS, 20CuTMS, and 25CuTMS after catalytic CO oxidation and the XRD patterns of 20CuTMS after stability test.

3.3. Study of in-situ FTIR

In-situ FTIR spectroscopy was performed to analyze the effects of temperature and active sites of CuTMS on catalytic CO oxidation (Fig. 7). The in-situ IR spectrum was obtained at the equivalent flux of CO and O_2 mixed with argon within the temperature range of 50 °C-250 °C. In-situ FTIR spectroscopy results showed that small amounts of CO adsorbed onto TMS and formed strong adsorption bands at 2335 and 2360 cm^{-1}, which could be assigned to the adsorbed CO_2 (Li et al., 2009; Heo et al., 2018). These two peaks appeared immediately after introducing the reaction gas at 50 °C and did not markedly change with changes in reaction temperature (Dong et l., 2016). The in situ FTIR spectra of TMS are shown in Fig. S7. The intensity of the bands of CuTMS materials at 2335 and 2360 cm^{-1} was almost consistent (Figs. 7a-c). According to the spectra of 10CuTMS, 20CuTMS, and 25CuTMS, the adsorption bands within the range of 2160-2080 cm^{-1} were attributed to Cu^{+}-CO (Schumann et al., 2017). Among the peak groups, a small shoulder was observed at 2080 cm^{-1} at low temperatures. This finding was consistent with that of Hikov et al. (2006), who reported that Cu(0) attaches to a TiO_2 surface. The peak of Cu(0)-CO was due to the reduction of Cu^{+}, which is typical of copper-stepped surfaces (labeled as peak α) (Boccuzzi and Chiorino, 1996; Wang et al., 2012). The main characteristic band located at 2130 cm^{-1} indicated the formation of

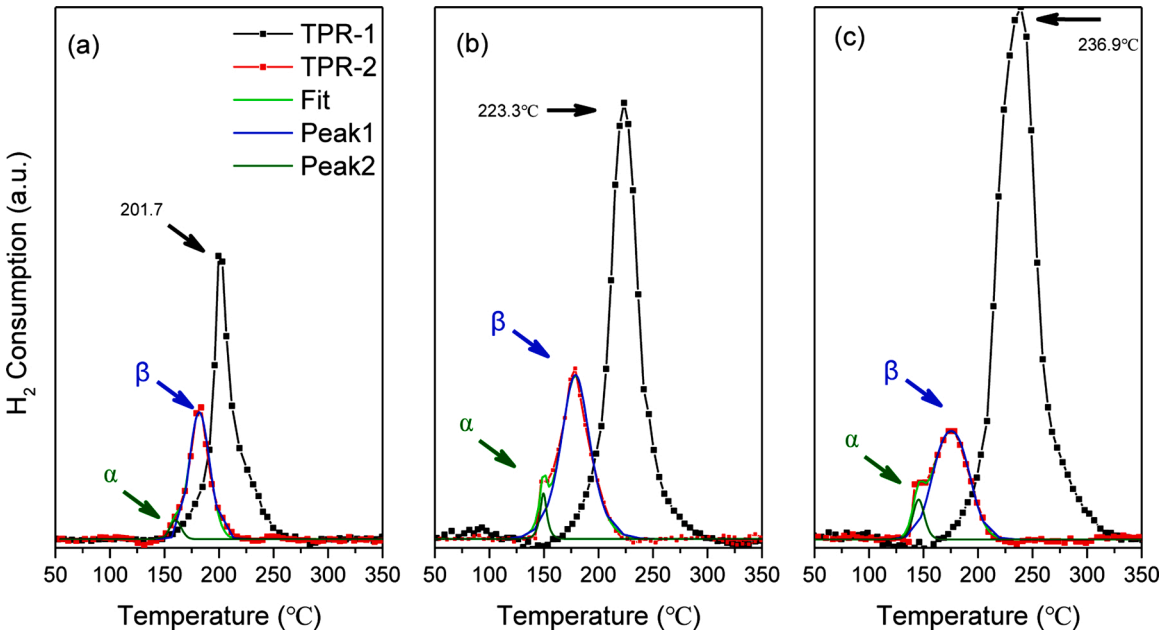

Fig. 8. H_2-TPRanalysis of (a) 10CuTMS, (b) 20CuTMS, and (c) 25CuTMS. The black curve is the result of the first H_2-TPR, whereas the red deconvoluted curve represents the hydrogen consumption after titration with N_2O.

Table 3
Estimated physicochemical properties of CuTMS by N_2O titration-assisted H_2-TPR.

Sample	peak α (℃)	peak β (℃)	Area α (a.u.)	Area β (a.u.)	D_{Cu} (in %)[a]	S_{Cu} (m^2/g_{Cu})[b]	S_{Cu} (m^2/g_{cat})[b]	d_{Cu} (in nm)[c]
10CuTMS	159.6	181.8	18.54	184.04	83.65	565.88	5.66	1.2
20CuTMS	149.8	179.2	22.62	327.16	79.21	535.86	10.72	1.3
25CuTMS	145.4	175.2	31.19	246.84	41.10	278.05	6.95	2.4

[a] $D_{Cu} = 2Y/X*100\%$.
[b] $S_{Cu} \approx 1353\ Y/X$.
[c] $d_{Cu} = 6/(S_{Cu}\rho_{Cu})$.

carbonyls, which were associated with isolated Cu oxide (labeled as peak β) (Boccuzzi and Chiorino, 1996). The disappearance of the bond group following the increase in reaction temperature was due to the removal of adsorbed CO. This phenomenon was highly related to reaction temperature, which occurred within the temperature range of 70 °C-90 °C in 20CuTMS and 90 °C-130 °C in 10CuTMS and 25CuTMS. The long-term stability of the material might be attributed to the rapid removal of the adsorbed CO without visible CO and CO_2 accumulation on the material surface, thereby preventing competition for and blocking the active sites (Szanyi and Kwak, 2014).

In-situ FTIR spectroscopy results indicated that the performance of the active sites was highly related to working temperature. However, these results combined with those of XPS showed that neither the ratio of Ti(III)/Ti(IV) nor the estimated Cu(β)/Cu(α + β) did not provide enough evidence to demonstrate that the performance and long-term stability of the materials improved.

3.4. *Effect of Active sites*

The study of the active sites for catalytic CO oxidation of copper-based materials are still under debate. Hydrogen TPR was performed to determine the reduction ability, particle size, and dispersion of copper and better understand the catalytic CO oxidation capability of CuTMS. The first H_2-TPR peak in Fig. 8 represents the total hydrogen consumption. TMS did not show a clear reduction peak at temperatures below 350 °C (not shown for brevity). The redox temperatures of 10CuTMS, 20CuTMS, and 25CuTMS were 201 °C, 222 °C, and 236 °C, respectively. Thus, an increase in hydrogen consumption was related to an increase in copper content. Meanwhile, the shift in reduction peaks toward elevated temperatures was due to the large particle size of copper. However, H_2-TPR-1 results showed all the prepared copper samples were equipped with one reduction peak only, and these samples were difficult to assign to a specific copper species (Xue et al., 2013). Coincidentally, all the reduction peaks located below 250 °C were related to highly dispersed copper (Zedan et al., 2017; Marchi et al., 1996). The second H_2-TPR was implemented after N_2O exposure. The results were used to calculate the average particle size, specific surface area, and dispersion of copper (Table 3). During the reduction, the uptake of H_2 was located within the temperature range of 125 °C-225 °C. The existence of a shoulder at the second reduction peak indicated different sites of copper, which could be deconvoluted into two peaks (peaks α and β). Peak α at about 150 °C corresponded to isolated copper oxides, whereas peak β at about 180 °C, which was assigned to copper in the TiO_2 framework, contributed to the Cu-O-Ti structure.

As shown in Table 3, the copper ions in 10CuTMS and 20CuTMS exhibited high dispersion of 83.65% and 79.21%, respectively. The remarkable decrease in dispersion in 25CuTMS (41.10%) was due to the large particle size of copper. The particle size of copper after further calculation was 1.2, 1.3, and 2.3 nm for 10CuTMS, 20CuTMS, and 25CuTMS, respectively. The result shows the particle size of the isolated copper oxide is less than 2.5 nm. That is consistent with no measurable Cu_2O or CuO diffraction peaks in the XRD spectrum.

Copper species can contribute to the active sites of catalytic CO oxidation. TOF calculation was performed to evaluate the effects of

Table 4
Effect of estimated active sites of α and β according to the deconvolution result of H_2-TPR-2.

$TOF_{70°C}$ (s^{-1} 10^{-3})	$TOF_{\alpha\text{-}70°C}$ ($s^{-1}10^{-3}$)	$TOF_{\beta\text{-}70°C}$ ($s^{-1}10^{-3}$)	$TOF_{130°C}$ ($s^{-1}10^{-3}$)	$TOF_{\alpha\text{-}130°C}$ ($s^{-1}10^{-3}$)	$TOF_{\beta\text{-}130°C}$ ($s^{-1}10^{-3}$)
3.00E-01	2.74E-02	2.72E-01	2.83E+00	2.59E-01	2.57E+00
1.69E-01	1.09E-02	1.58E-01	7.98E+00	5.16E-01	7.46E+00
5.14E-02	5.76E-03	4.56E-02	4.39E+00	4.93E-01	3.90E+00

different active sites (Xue et al., 2013). TOF reflects the active sites of surface copper that convert the number of molecules of CO in a unit reaction time to obtain the specific catalyst activity. In situ FTIR results showed that the CO conversion rate consisted of conversion at 70 °C and 130 °C for estimating TOF (Guo and Vlachos, 2015). The estimated effects of the active sites was based on the deconvolution result of H_2-TPR-2 to identify the ratio of two sites of isolated copper oxide and Cu-O-Ti.

$TOF_{sites\text{-}temperature}$ is summarized in Table 4. The α-type active site, which was the ratio of different active sites, provided almost stable catalytic CO oxidation ability at various temperatures. Therefore, the peak β-type of copper species with a Cu-O-Ti structure exhibited the best catalytic CO oxidation performance. Interestingly, the estimated $TOF_{\beta\text{-}70}$ and $TOF_{\beta\text{-}130}$ followed the order 20CuTMS ≈ 10CuTMS > 25CuTMS and 20CuTMS > 25CuTMS > 10CuTMS, respectively. This phenomenon was strongly related to the result of catalytic CO oxidation (Fig. 5).

4. Conclusion

In this work, we developed a well-dispersed CuTMS material with long-term stability for catalytic CO oxidation. This material was synthesized via a facile one-step AASA process. Real-time mass spectrum analysis and in-situ techniques were performed to investigate the active sites of copper and their contribution to the stability of CuTMS material. In the catalytic CO oxidation reaction, CuTMS exhibited complete oxidation of CO to CO_2 with a wide working temperature range and also showed excellent stability under extreme conditions (GHSV = 100,000 h^{-1}, 250 °C at 200 h). The active sites played a crucial role in catalytic CO oxidation. In-situ FTIR spectroscopy and N_2O titration-assisted H_2-TPR results revealed two active copper species that were assigned to well-dispersed thin particles of isolated CuO and incompletely coordinated copper introduced into the TiO_2 framework of Cu-O-Ti. These results combined with those of catalytic CO oxidation conversion versus temperature revealed that the effects of the active sites were determined by the reaction temperature. In this case, the isolated CuO displayed an outstanding performance for catalytic CO oxidation at relatively low temperatures. The large amounts of Cu-O-Ti types of copper played a dominant role in catalytic CO oxidation. Notably, the removal of the surface binding group (2130 cm^{-1}) indicated the working temperature of different active sites. H_2-TPR provided information regarding the active sites and the internal copper exposure sites. CuTMS holds great application potential in three-way converters for removing CO in industrial smokestacks and automobile exhausts.

CRediT authorship contribution statement

Wen-Ta Yang: Writing - original draft, Methodology, Software. **Chin Jung Lin:** Visualization, Investigation. **Tiziano Montini:** Methodology. **Paolo Fornasiero:** Supervision. **Sofia Ya:** Conceptualization, Supervision, Writing - review & editing. **Sofia Ya Hsuan Liou:** Conceptualization, Supervision, Writing - review & editing.

Declaration of Competing Interest

The authors report no declarations of interest.

Acknowledgements

This work was financially supported by EURASIACAT: Advanced Education European-Asiatic Exchange Program in Materials Science and Catalysis, NTU Research Center for Future Earth from The Featured Areas Research Center Program within the framework of the Higher Education Sprout Project by the Ministry of Education (MOE) in Taiwan and the Ministry of Science and Technology Taiwan (MOST 108-2116-M-002-020).

Appendix A. Supplementary data

Supplementary material related to this article can be found, in the online version, at doi:https://doi.org/10.1016/j.jhazmat.2020.123630.

References

Bharti, B., Kumar, S., Lee, H., Kumar, R., 2016. Formation of oxygen vacancies and Ti^{3+} state in TiO_2 thin film and enhanced optical properties by air plasma treatment. Sci. rep. 6, 32355. https://doi.org/10.1038/srep32355.

Choudhury, Biswajit, Dey, Munmun, Choudhury, Amarjyoti, 2013. Defect generation, d-d transition, and band gap reduction in Cu-doped TiO_2 nanoparticles. Int. Nano Lett 3, 25, 0.1186/2228-5326-3-25.

DeRita, L., Dai, S., Lopez-Zepeda, K., Pham, N., Graham, G.W., Pan, X., Christopher, P., 2017. Catalyst architecture for stable single atom dispersion enables site-specific spectroscopic and reactivity measurements of CO adsorbed to Pt atoms, oxidized Pt clusters, and metallic Pt clusters on TiO_2. J. Am. Chem. Soc. 139, 14150–14165. https://doi.org/10.1021/jacs.7b07093.

DeSario, P.A., Pitman, C.L., Delia, D.J., Driscoll, D.M., Maynes, A.J., Morris, J.R., Pennington, A.M., Brintlinger, T.H., Rolison, D.R., Pietron, J.J., 2019. Low-temperature CO oxidation at persistent low-valent Cu nanoparticles on TiO_2 aerogels. App. Cat. B: Env. 252, 205–213. https://doi.org/10.1016/j.apcatb.2019.03.073.

Dong, L., Tang, Y., Li, B., Zhou, L., Gong, F., He, H., Sun, B., Tang, C., Gao, F., Dong, l., 2016. Influence of molar ratio and calcination temperature on the properties of $TixSn_{1-x}O_2$ supporting copper oxide for CO oxidation. App. Cat. B: Env. 180, 451–462. https://doi.org/10.1016/j.apcatb.2015.06.034.

Gao, J., Jia, C., Zhang, L., Wang, H., Yamg, Y., Hung, S.-F., Hsu, Y.-Y., Liu, B., 2016. Tuning chemical bonding of MnO2 through transition-metal doping for enhanced CO oxidation. J. Cat. 341, 82–90. https://doi.org/10.1016/j.jcat.2016.06.009.

Gervasini, A., Bennici, S., 2005. Dispersion and surface states of copper catalysts by temperature-programmed-reduction of oxidized surfaces (s-TPR). App. Cat. A: Gen. 281, 199–205. https://doi.org/10.1016/j.apcata.2004.11.030.

Guan, H., Lin, J., Qiao, B., Yang, X., Li, L., Miao, S., Liu, J., Wang, A., Wang, X., Zhang, T., 2016. Catalytically Active Rh Sub-Nanoclusters on TiO_2 for CO Oxidation at Cryogenic Temperatures Ange. Chem. Int. Ed. 55, 2820–2824. https://doi.org/10.1002/anie.201510643.

Guo, W., Vlachos, D.G., 2015. Patched bimetallic surfaces are active catalysts for ammonia decomposition. Nat. comm. 6, 1–7. https://doi.org/10.1038/ncomms9619.

Hampsey, J.E., Arsenault, S., Hu, Q., Lu, Y., 2005. One-Step Synthesis of Mesoporous Metal− SiO_2 Particles by an Aerosol-Assisted Self-assembly Process. Chem. Mat. 17, 2475–2480, 10.1021/cm0487167.

Heo, I., Schmieg, S.J., Oh, S.H., Li, W., Peden, C.H., Kim, C.H., Szanyi, J., 2018. Improved thermal stability of a copper-containing ceria-based catalyst for low temperature CO oxidation under simulated diesel exhaust conditions. Cat. Sci. & Tech. 8, 1383–1394. https://doi.org/10.1039/C7CY02288C.

Kaminski, P., Ziolek, M., Campo, B., Daturi, M., 2015. FTIR spectroscopic study of CO oxidation on bimetallic catalysts. Cat. Tod. 243, 218–227. https://doi.org/10.1016/j.cattod.2014.08.035.

Kim, H.Y., Liu, P., 2015. Complex Catalytic Behaviors of $CuTiO_x$ Mixed-Oxide during CO Oxidation. J. Phy. Chem. C 119, 22985–22991. https://doi.org/10.1021/acs.jpcc.5b07099.

Kwak, J.H., Hu, J., Mei, D., Yi, C.-W., Kim, D.H., Peden, C.H., Allard, L.F., Szanyi, J., 2009. Coordinatively unsaturated Al^{3+} centers as binding sites for active catalyst phases of platinum on γ-Al_2O_3. Science 325, 1670–1673. https://doi.org/10.1126/science.1176745.

Lai, N.-C., Tsai, M.-C., Liu, C.-H., Chen, C.-S., Yang, C.-M., 2018. Efficient selective oxidation of propylene by dioxygen on mesoporous-silica-nanoparticle-supported nanosized copper. J. Cat. 365, 411–419. https://doi.org/10.1016/j.jcat.2018.07.014.

Lee, S., Fan, C., Wu, T., Anderson, S.L., 2005. Agglomeration, support effects, and CO adsorption on Au/TiO2 (1 1 0) prepared by ion beam deposition. Sur. Sci. 578, 5–19. https://doi.org/10.1016/j.susc.2005.01.017.

Lee, S., Jeong, S., Kim, W.D., Lee, S., Lee, K., Bae, W.K., Moon, J.H., Lee, S., Lee, D.C., 2016. Low-coordinated surface atoms of CuPt alloy cocatalysts on TiO_2 for enhanced photocatalytic conversion of CO_2. Nanos 8, 10043–10048. https://doi.org/10.1039/C6NR02124G.

Li, L., Li, W., Zhu, C., Mao, L.-F., 2020. The effect of oxygen vacancy at CO oxidation on anatase (001)-supported single-Au catalyst. Mat. Chem. Phy 240, 122291. https://doi.org/10.1016/j.matchemphys.2019.122291.

Li, M., Wu, Z., Ma, Z., Schwartz, V., Mullins, D.R., Dai, S., Overbury, S.H., 2009. CO oxidation on Au/FePO4 catalyst: Reaction pathways and nature of Au sites. J. Cat. 266, 98–105. https://doi.org/10.1016/j.jcat.2009.05.019.

Lin, C.-J., Yang, W.-T., 2014. Ordered mesostructured Cu-doped TiO_2 spheres as active visible-light-driven photocatalysts for degradation of paracetamol. Chem. Eng. J. 237, 131–137. https://doi.org/10.1016/j.cej.2013.10.027.

Lin, L.-Y., Wang, C., Bai, H., 2015. A comparative investigation on the low-temperature catalytic oxidation of acetone over porous aluminosilicate-supported cerium oxides. Chem. Eng. J. 264, 835–844. https://doi.org/10.1016/j.cej.2014.12.042.

Liu, K., Wang, A., Zhang, T., 2012. Recent advances in preferential oxidation of CO reaction over platinum group metal catalysts. ACS cat. 2, 1165–1178. https://doi.org/10.1021/cs200418w.

Lu, Schwank, 1999. Aerosol-assisted self-assembly of mesostructured spherical nanoparticles. Nat. 398, 223–226. https://doi.org/10.1038/18410.

Ma, L., Chen, X., Li, J., Chang, H., Schwank, J.W., 2019. Electronic Metal-Support Interactions in Pt/FeO_x Nanospheres for CO Oxidation. Cat. Tod. https://doi.org/10.1016/j.cattod.2019.06.055.

Marchi, A., Fierro, J., Santamaría, J., Monzon, A., 1996. Dehydrogenation of isopropylic alcohol on a Cu/SiO_2 catalyst: a study of the activity evolution and reactivation of the catalyst. App. Cat. A: Gen. 142, 375–386. https://doi.org/10.1016/0926-860X(96)00087-7.

Mehrmohammadi, M., Qu, M., Ma, L.L., Romanovicz, D.K., Johnston, K.P., Sokolov, K.V., Emelianov, S.Y., 2011. Pulsed magneto-motive ultrasound imaging to detect intracellular accumulation of magnetic nanoparticles. Nanot. 22, 415105. https://doi.org/10.1088/0957-4484/22/41/415105.

Mo, S., He, H., Ren, Q., Li, S., Zhang, W., Fu, M., Fu, Chen, Wu, J., Chen, Y., Ye, D., 2019. Macroporous Ni foam-supported Co_3O_4 nanobrush and nanomace hybrid arrays for high-efficiency CO oxidation. J. Env. Sci. 75, 136–144. https://doi.org/10.1016/j.jes.2018.02.026.

Murata, K., Eleeda, E., Ohyama, J., Yamamoto, Y., Arai, S., Satsuma, A., 2019. Identification of active sites in CO oxidation over a Pd/Al_2O_3 catalyst. Phy. Chem. Chem. Phy 21, 18128–18137. https://doi.org/10.1039/c9cp03943k.

Naldoni, A., Allieta, M., Santangelo, S., Marelli, M., Fabbri, F., Cappelli, S., Bianchi, C.L., Psaro, R., Santo, V.D., 2012. Effect of nature and location of defects on bandgap narrowing in black TiO_2 nanoparticles. J. Am. Chem. Soc. 134, 7600–7603. https://doi.org/10.1021/ja3012676.

Newton, M.A., Ferri, D., Smolentsev, G., Marchionni, V., Nachtegaal, M., 2015. Room-temperature carbon monoxide oxidation by oxygen over Pt/Al_2O_3 mediated by reactive platinum carbonates. Nat. comm. 6, 1–7. https://doi.org/10.1038/ncomms9675.

Nie, L., Mei, D., Xiong, H., Peng, B., Ren, Z., Hernandez, X.I.P., DeLaRiva, A., Wang, M., Engelhard, M.H., Kovarik, L., 2017. Activation of surface lattice oxygen in single-atom Pt/CeO_2 for low-temperature CO oxidation. Science 358, 1419–1423. https://doi.org/10.1126/science.aao2109.

Park, M.B., Ahn, S.H., Mansouri, A., Ranocchiari, M., van Bokhoven, J.A., 2017. Comparative study of diverse copper zeolites for the conversion of methane into methanol. Chem. Cat. Chem. 9, 3705–3713. https://doi.org/10.1002/cctc.201700768.

Pham, T.-D., Lee, B.-K., 2016. Advanced removal of C. famata in bioaerosols by simultaneous adsorption and photocatalytic oxidation of Cu-doped TiO_2/PU under visible irradiation. Chem. Eng. J. 286, 377–386. https://doi.org/10.1016/j.cej.2015.10.100.

Putrakumar, B., Nagaraju, N., Kumar, V.P., Chary, K.V., 2015. Hydrogenation of levulinic acid to γ-valerolactone over copper catalysts supported on γ-Al_2O_3. Cat. Tod. 250, 209–217. https://doi.org/10.1016/j.cattod.2014.07.014.

Ryu, J., Kim, S., Kim, H.I., Jo, E.-H., Kim, Y.K., Kim, M., Jang, H.D., 2015. Self-assembled TiO_2 agglomerates hybridized with reduced-graphene oxide: A high-performance hybrid photocatalyst for solar energy conversion. Chem Eng. J. 262, 409–416. https://doi.org/10.1016/j.cej.2014.10.001.

Schumann, J., Köhnert, J., Frei, E., Schlögl, R., Trunschke, A., 2017. IR-spectroscopic study on the interface of Cu-based methanol synthesis catalysts: evidence for the formation of a ZnO overlayer. Top. Cat. 60, 1735–1743. https://doi.org/10.1007/s11244-017-0850-9.

Seo, P.W., Choi, H.J., Hong, S.I., Hong, S.C., 2010. A study on the characteristics of CO oxidation at room temperature by metallic Pt. J. Haz. Mat. 178, 917–925. https://doi.org/10.1016/j.jhazmat.2010.02.025.

Seriani, N., Pinilla, C., Crespo, Y., 2015. Presence of gap states at Cu/TiO_2 anatase surfaces: consequences for the photocatalytic activity. J. Phy. Chem. C 119, 6696–6702. https://doi.org/10.1021/acs.jpcc.5b00846.

Shokouhimehr, M., Hong, K., Lee, T.H., Moon, C.W., Hong, S.P., Zhang, K., Suh, J.M., Choi, K.S., Varma, R.S., Jang, H.W., 2018. Magnetically retrievable nanocomposite adorned with Pd nanocatalysts: efficient reduction of nitroaromatics in aqueous media. G. chem. 20, 3809–3817. https://doi.org/10.1039/C8GC01240G.

Srivastava, A.K., Saxena, A., Shah, D., Mahato, T., Singh, B., Shrivastava, A., Gutch, P., Shinde, C., 2012. Catalytic removal of carbon monoxide over carbon supported palladium catalyst. J. Haz. Mat. 241, 463–471. https://doi.org/10.1016/j.jhazmat.2012.10.001.

Suchomel, P., Kvitek, L., Prucek, R., Panacek, A., Halder, A., Vajda, S., Zboril, R., 2018. Simple size-controlled synthesis of Au nanoparticles and their size-dependent catalytic activity. Sci. rep. 8, 1–11. https://doi.org/10.1038/s41598-018-22976-5.

Svintsitskiy, D.A., Kardash, T.Y., Stonkus, O.A., Slavinskaya, E.M., Stadnichenko, A.I., Koscheev, S.V., Chupakhin, A.P., Boronin, A.I., 2013. In situ XRD, XPS, TEM, and TPR study of highly active in CO oxidation CuO nanopowders. J. Phy. Chem. C 117, 14588–14599. https://doi.org/10.1021/jp403339r.

Szanyi, J., Kwak, J.H., 2014. Dissecting the steps of CO_2 reduction: 2. The interaction of CO and CO_2 with Pd/γ-Al_2O_3: an in situ FTIR study. Phy. Chem. Chem. Phy. 16, 15126–15138. https://doi.org/10.1039/C4CP00617H.

Tang, Y., Dong, L., Deng, C., Huang, M., Li, B., Zhang, H., 2016. In situ FT-IR investigation of CO oxidation on CuO/TiO_2 catalysts. Cat. Comm. 78, 33–36. https://doi.org/10.1002/anie.200802487.

Tsung, C.K., Fan, J., Zheng, N., Shi, Q., Forman, A.J., Wang, J., Stucky, G.D., 2008. A general route to diverse mesoporous metal oxide submicrospheres with highly crystalline frameworks. Ang. Chem. Int. Ed. 47, 8682–8686. https://doi.org/10.1002/anie.200802487.

Wang, D., Kan, Y., Yu, X., Liu, J., Song, L., Hu, Y., 2016. In situ loading ultra-small Cu_2O nanoparticles on 2D hierarchical TiO_2-graphene oxide dual-nanosheets: Towards reducing fire hazards of unsaturated polyester resin. J. Haz. Mat. 320, 504–512. https://doi.org/10.1016/j.jhazmat.2016.08.066.

Xu, Y., Wu, S., Wan, P., Sun, J., Hood, Z.D., 2017. Introducing Ti^{3+} defects based on lattice distortion for enhanced visible light photoreactivity in TiO_2 microspheres. RSC Adv. 7, 32461–32467. https://doi.org/10.1039/C7RA04885H.

Xue, J., Wang, X., Qi, G., Wang, J., Shen, M., Li, W., 2013. Characterization of copper species over Cu/SAPO-34 in selective catalytic reduction of NO_x with ammonia: Relationships between active Cu sites and de-NO_x performance at low temperature. J. Cat. 297, 56–64. https://doi.org/10.1016/j.jcat.2012.09.020.

Luo, Y., Zheng, Y., Zuo, J., Feng, X., Wang, X., Zhang, T., Zhang, K., Jiang, L., 2018. Insights into the high performance of Mn-Co oxides derived from metal-organic frameworks for total toluene oxidation. J. Haz. Mat. 349, 119–127. https://doi.org/10.1016/j.jhazmat.2018.01.053.

Zedan, A.F., Allam, N.K., AlQaradawi, S.Y., 2017. Temperature CO Oxidation over Mesoporous CuO-TiO_2 Nanotube Catalysts. Catalysts 7, 129. https://doi.org/10.3390/catal7050129.

Zeng, Y., Wang, T., Zhang, S., Wang, Y., Zhong, Q., 2017. Sol–gel synthesis of CuO-TiO_2 catalyst with high dispersion CuO species for selective catalytic oxidation of NO. App. Sur. Sci. 411, 227–234. https://doi.org/10.1016/j.apsusc.2017.03.107.

Zhang, L.-L., Sun, M.-J., Liu, andC.-G., 2019. CO oxidation on the phosphotungstic acid supported Rh single–atom catalysts via Rh–assisted Mans–van Krevelen mechanism. Mol. Cat. 462, 37–45. https://doi.org/10.1016/j.mcat.2018.10.017.

Zhang, R., Hu, L., Bao, S., Li, R., Gao, L., Li, R., Chen, Q., 2016. Surface polarization enhancement: high catalytic performance of Cu/CuO_x/C nanocomposites derived from Cu-BTC for CO oxidation. J. Mat. Chem. A 4, 8412–8420. https://doi.org/10.1039/C6TA01199C.

Zhang, W., Li, Y., Zhu, S., Wang, F., 2004. Copper doping in titanium oxide catalyst film prepared by dc reactive magnetron sputtering. Cat. Tod. 93, 589–594. https://doi.org/10.1016/j.cattod.2004.06.009.